applied optics

On-chip membrane-based GaInAs/InP waveguide-type *p-i-n* photodiode fabricated on silicon substrate

Zhichen Gu,[1,*] Tatsuya Uryu,[1] Nagisa Nakamura,[1] Daisuke Inoue,[1] Tomohiro Amemiya,[2] Nobuhiko Nishiyama,[1,2] and Shigehisa Arai[1,2]

[1]Department of Electrical and Electronic Engineering, Tokyo Institute of Technology, Meguro-ku, Tokyo 152-8552, Japan
[2]Institute of Innovative Research, Tokyo Institute of Technology, Meguro-ku, Tokyo 152-8552, Japan
*Corresponding author: gu.z.ab@m.titech.ac.jp

Received 18 July 2017; revised 30 August 2017; accepted 30 August 2017; posted 5 September 2017 (Doc. ID 302766); published 25 September 2017

Toward the realization of ultralow-power-consumption on-chip optical interconnection, two types of membrane-based GaInAs/InP *p-i-n* photodiodes were fabricated on Si host substrates by using benzocyclobutene bonding. A responsivity of 0.95 A/W was estimated with a conventional waveguide-type photodiode with an ∼30-μm-long absorption region. The fitting curves based on the experimental data indicated that an absorption efficiency above 90% could be achieved with a length of 10 μm. In addition, increased absorption per length of a photonic crystal waveguide-type photodiode was obtained because of the enhanced lateral optical confinement or the slow-light effect, enabling a further reduction in the device length. © 2017 Optical Society of America

OCIS codes: (050.5298) Photonic crystals; (130.5990) Semiconductors; (200.4650) Optical interconnects; (230.5160) Photodetectors.

https://doi.org/10.1364/AO.56.007841

1. INTRODUCTION

Enhancements in the density and performance of large-scale integrated (LSI) circuits have fueled the semiconductor industry and have resulted in the explosive growth of the information-processing technology for decades. However, the fundamental limitations of copper-based interconnects in global wire layers (e.g., signal delay, Joule heating, crosstalk, power dissipation, etc.) have been considered critical factors hampering the further development of LSI based on the miniaturization of transistors. Research groups continued to pursue new solutions for the interconnection functional blocks, such as three-dimensional integrated circuits based on a through-silicon via [1], wireless capacitive coupling [2], or inductive coupling [3]. Apart from these, the on-chip optical interconnection has been attracting worldwide attention in recent years because of its significant potential for data capacity and power saving. In order to continue the development of electronics, it has been reported that the on-chip optical interconnection should be able to handle a data rate of 10 Gb/s with a total system energy cost of much less than 100 fJ/bit [4]. Si photonics is considered a strong candidate for such high-performance on-chip photonic integrated circuits because of its compatibility with the mature CMOS technology [5,6]. Recently, research activities have focused on the combination of Si and III–V compound photonic devices by using low-temperature direct growth or hybrid bonding technologies for compensating the insufficient light-emitting capacity of Si when it is used as an indirect bandgap material [7,8]. In parallel with this trend, the use of an InP-based monolithic integration platform of membrane devices as an ultralow-power-consumption on-chip optical interconnection has also been proposed [9,10]. Such a membrane photonic integrated circuit (MPIC) can also be introduced into the CMOS LSI in a back-end-of-line process by using the bonding technology. Compared with conventional III–V laser diodes, the membrane structure consists of a thin core layer (200–300 nm) sandwiched between two low-refractive-index dielectric cladding layers, such as air, SiO_2, or benzocyclobutene (BCB), instead of a semiconductor. The large refractive index difference results in the enhancement of optical confinement in the active region, increasing the modal gain and thereby enabling an ultralow-threshold current operation. It should be noted that a lateral-current-injection structure is required for the electrical pumping of membrane devices [11]. In addition, a further-miniaturized active layer within a distributed-feedback or distributed-reflector laser can be realized by introducing a surface grating structure, which results in an enhanced index-coupling coefficient of the membrane structure [12,13].

The membrane photodiode (PD) is another key component of the MPIC, which should be able to match the modulation

speed of the laser diode with extremely small energy consumption. Recently, the concept of "receiverless PD" could be verified because of the mature semiconductor processing technology [14,15]. A sufficient voltage signal that can be identified by the subsequent LSI circuit should be obtained from the terminal of the MPIC by combining the PD with a high-load resistor instead of electrical amplifiers, such as transimpedance amplifiers, which are usually adopted in conventional receivers [16,17]. Thereby, the energy cost during the opto/electric signal conversion can be reduced from pJ/bit to fJ/bit level with an assumed data rate of 10 Gb/s. In addition, the Johnson noise of the PDs can be theoretically reduced by combining a high-load resistor, which will increase the sensitivity of the PD and lower the required overall power consumption of the optical link because of the reduction in the output power required for the laser source. In this case, an ultra-compact PD with an extremely small junction capacitance is required for lowering the resistance-capacitance (RC) constant so that a high-level cutoff frequency can be maintained. Among all the candidates for on-chip PDs, such as Ge-waveguide PD [18], Ge Avalanche PD [19], nanowire PD [20], nanopillar PD [21], or plasmonic PD [22], we considered the GaInAs/InP waveguide-type PD as the most promising solution for being compatible with the MPIC, which requires a lateral *p-i-n* junction. The membrane-based GaInAs-bulk PD can provide a high responsivity to 1550-nm wavelength light with a shortened device length because of the enhanced optical confinement in the vertical direction. Moreover, it was recently reported that further reduction in the device length could be realized by introducing a photonic crystal (PhC) structure in the absorption region, which will induce either the enhancement of the lateral optical confinement or the slow-light effect [23–25].

Several studies of membrane-type PDs have been conducted in the past few years, which include studies on the GaInAsP/InP multi-quantum well (MQW) [26] and bulk-GaInAs absorption-layer-based LCI-PD on semi-insulator-InP substrate [27]. In addition, a membrane MQW-PD formed on a Si substrate has been demonstrated recently as a component of the monolithic integrated circuit [28]. In this work, we report a membrane bulk-GaInAs/InP waveguide PD with higher responsivity and shortened device length compared to the former devices. In addition, both the calculation result based on the 3D finite-difference time domain (FDTD) method and fitting curves of the experimental data indicated that a further reduction in the device length could be realized by introducing an in-plane PhC structure.

2. DEVICE STRUCTURE AND PROCESS FLOW

Figure 1 shows the schematics of the GaInAs/InP *p-i-n* waveguide-type membrane PD bonded on a Si substrate; detailed layer structures of the photodiode region and the waveguide region are noted below. A 120-nm-thick GaInAs bulk is sandwiched laterally between *n*-InP and *p*-InP side clads, which also forms a lateral *p-i-n* junction, and vertically between a top 100-nm-thick *p*-InP clad and a bottom 50-nm-thick *u*-InP clad, as shown in the layer structure (exactly the same layer structure as that of the membrane laser except for the active region). The PD is connected with a 155-nm-thick GaInAsP (λ_g = 1220 nm)-core-layer waveguide using a butt-jointed built-in

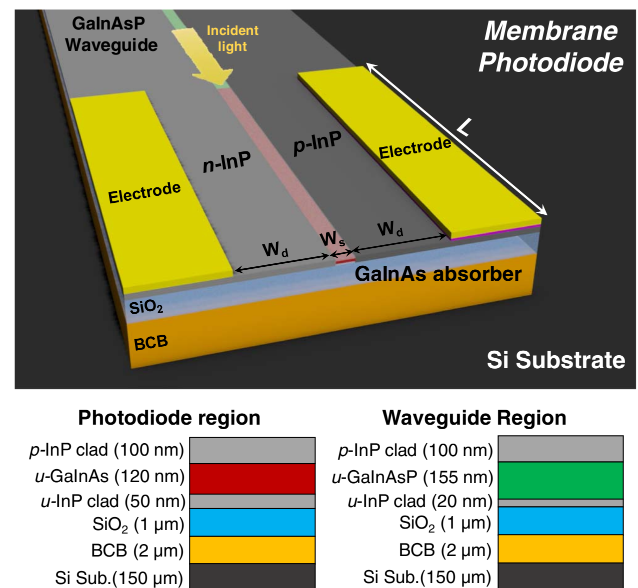

Fig. 1. Schematics of GaInAs/InP *p-i-n* membrane PD bonded on Si substrate using BCB.

structure, which would also be adopted for connecting other membrane devices in the MPIC. The fabrication process was compatible with the procedure of the entire membrane optical link, as we have reported before [29], where a mature etching and regrowth technology based on organo-metallic vapor-phase-epitaxy (OMVPE) and UV photolithography were performed for embedding the GaInAs absorber and GaInAsP core inside the InP clads. The device fabrication was initiated by the formation of the GaInAs island on the *n*-InP substrate based on a selective etching process using a SiO_2 mask. Then the passive waveguide layer was selectively regrown around the GaInAs island by the OMVPE. The GaInAsP core in the passive region was directly joined to the absorber. Next, a second-step selective regrowth of the *n*-InP and *p*-InP clad layers was performed to form a lateral *p-i-n* junction structure, which also provide a lateral optical confinement for both the waveguide region and the photodiode region. After the III–V regrowth process, a 1-μm-thick SiO_2 layer was deposited by plasma-enhanced chemical-vapor deposition; the wafer was then turned upside down and bonded to a Si host substrate using BCB adhesive bonding. The SiO_2 layer improved the reproducibility of our wafer-scale bonding process without formation of voids at the interface. Next, the membrane structure was formed by removing the *n*-InP substrate and the etch-stop layer using polishing and selective chemical etching, respectively. The 270-nm-thick core layer of the PD was then sandwiched between a top clad of air and a bottom clad of SiO_2. Subsequently, a p^+-GaInAs contact layer was formed on the *p*-InP section by removing the unnecessary region in the initial wafer with a 100-nm-thick SiO_2 mask, which was used for the remaining patterning process also. Ti/Au cross-metal marks used for the alignment of the electron-beam (EB) lithography were then deposited on the wafer by using EB evaporation. In the case of the PhC-waveguide-type PD, the air holes were then formed in the *p*- and *n*-InP sections right beside the GaInAs bulk by using 100-kV EB lithography

and $CH_4/H_2/Cl_2$ dry etching. The EB dose strength was 320 $\mu C/cm^2$. The PhC was designed with a lattice constant a of 420 nm and diameter d of 230 nm, as has been reported earlier [30]. Subsequently, a Ti/Au electrode was deposited on the n-InP section, and a Au/Zn/Au electrode was introduced for the p-electrode. The redundant SiO_2 mask was then removed by buffered hydrofluoric acid wet etching as the last step of the fabrication process. In this report, we fabricated both conventional-waveguide-type and PhC-waveguide-type PDs with different stripe widths W_s (0.5 μm, 0.7 μm, and 0.9 μm) and absorption region lengths L of the GaInAs bulk for verifying the relationship between them. The designed lengths of the GaInAs absorber in the photomask were 2.5–30 μm; however, it was confirmed after fabrication that the actual absorption length was shrunk by approximately 0.5 μm due to side etching. Moreover, it should be noted that the width of the PhC waveguide of PhC-PD is designed to be 0.4-μm wider than the stripe width W_s for suppressing the non-radiative carrier recombination loss, such as that due to surface recombination. The width of the n-InP and p-InP clad layers W_d, as the distance between the electrodes and the GaInAs absorber, was designed to be 5 μm this time for ensuring enough space for the formation of air holes.

Figure 2(a) shows the optical microscope image of the top view of one of the fabricated conventional-waveguide-type PDs. The designed length of the GaInAs absorber was 7.5 μm, which was connected with the GaInAsP waveguide on both sides in the propagation direction (measurement of the PD can be taken with an incident light in either direction). Figure 2(b) shows the SEM image of the cross-sectional view of the passive waveguide region. The GaInAsP core was well embedded between the p- and n-InP cladding layers (higher regrowth thickness) in the lateral direction, the stripe width of which was confirmed to be 0.7 μm. The stripe width of the

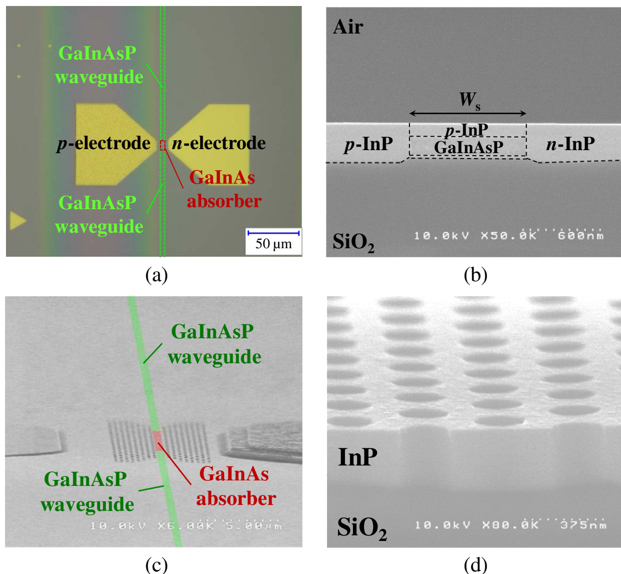

Fig. 2. (a) Microscope image of the fabricated conventional-waveguide-type PD. (b) SEM image of the cross-sectional view of the GaInAsP waveguide region. (c) SEM image of the photonic-waveguide-type PD. (d) Enlarged cross-sectional view of the PhC region.

passive waveguide was the same as the designed stripe width W_s of the GaInAs bulk. Figure 2(c) shows the SEM image of the PhC-waveguide-type PD, and Fig. 2(d) shows the enlarged view of the PhC region. A good verticality of the air-hole sidewall was confirmed. The diameter d and the lattice constant a were 230 nm and 420 nm, respectively, which were consistent with the design.

3. EXPERIMENTAL RESULTS AND ANALYSIS OF RESPONSIVITY

A. Conventional-Waveguide-Type GaInAs/InP *p-i-n* PD

Before the measurement of the devices, the fabricated wafer was cleaved into a bar form in the passive waveguide region. The cleaving was performed with the aid of an automated wafer scriber, and the distance between the facet and the PD was approximately 125 μm.

Figure 3 shows the schematic of the experimental setup for measuring the responsivity of the fabricated device. The transverse electric polarized light from a wavelength-tunable laser source was coupled with the passive GaInAsP waveguide connected to the PD by using a spherical-lensed single-mode polarization-maintaining fiber. Therefore, the measured responsivity R_{ex} of the PD based on this setting can be described by equation Eq. (1) as follows:

$$R_{\text{ex}} = \eta_f \cdot \eta_{\text{wg}} \cdot \eta_c \cdot \eta_{\text{i}} \cdot \frac{q}{h\nu} \cdot (1 - e^{-\xi\alpha L}), \tag{1}$$

where η_f is the coupling efficiency between the fiber and the passive waveguide, η_{wg} is the attenuation rate due to the propagation loss in the passive waveguide, η_c is the coupling efficiency between the waveguide and the PD, η_i is the loss factor that represents the loss of the photogenerated carrier (i.e., radiative or nonradiative recombination at the hetero interface), q is the electron charge, h is Planck's constant, and v is the frequency of light. The last term $(1 - \exp(-\xi\alpha L))$ represents the absorption efficiency of the PD, where ξ is the optical confinement factor, α is the absorption coefficient of GaInAs, and L is the absorber length. In this work, all the devices were assessed at a fixed wavelength of 1.55 μm in consideration of the designed lasing wavelength of the membrane laser in the MPIC.

Figure 4 shows the measured photocurrent I_{pd} against the input power P_{in} of a device with $L = 30$ μm and $W_s =$ 0.7 μm for different bias voltages, which indicate that R_{ex} is 0.19 A/W. The measured dark leakage current of this conventional-waveguide-type PD at a reverse bias of 1 V was found to be 5.5 μA, which is higher than the value of the

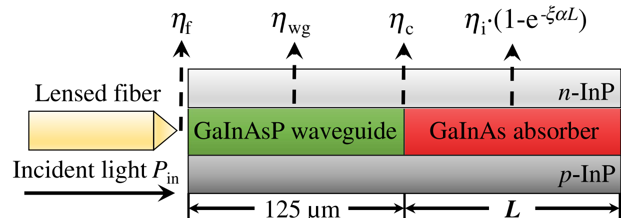

Fig. 3. Schematic figure of the experimental setup for measuring the responsivity of the waveguide-type PD.

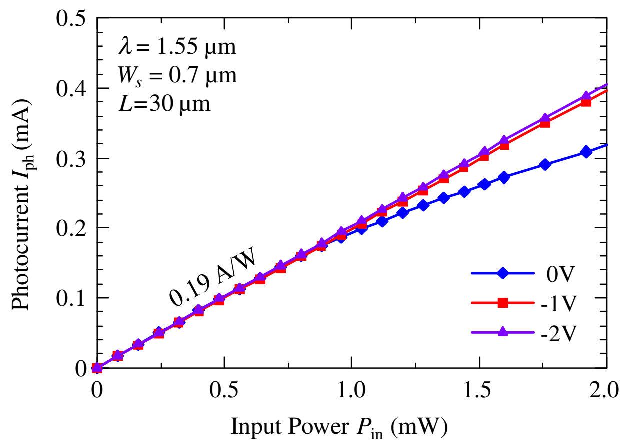

Fig. 4. Photocurrent against independent power at 1550 nm and different bias voltages.

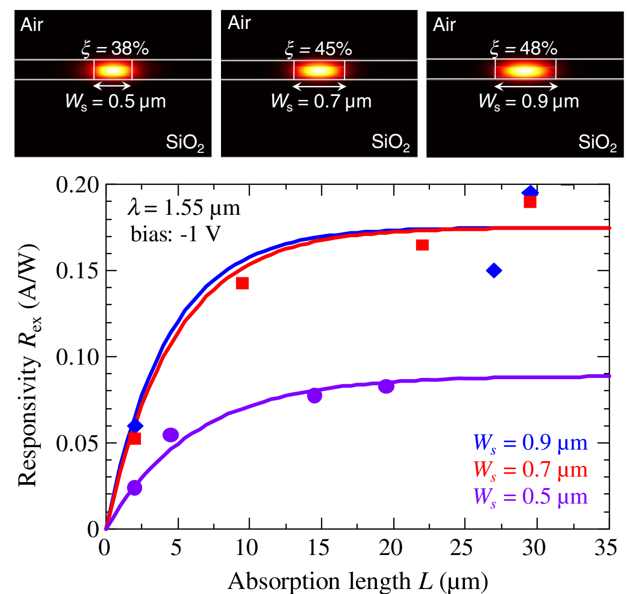

Fig. 5. Experimental plots and theoretical curves of R_{ex} of the conventional-waveguide-type PD against absorption length at 1.55 μm with different stripe widths W_s and the calculated mode field distribution.

formerly reported MQW-absorber-based PD. We are now investigating the reason for the increase of the dark current, which might be attributed to the crystal quality of the *i*-GaInAs. During the analysis, η_f should be excluded from the calculation of R_{ex} for assessing the responsivity of the device itself, as the light from the laser source will be directly incident on the passive-waveguide-connected PD in the case of MPIC. The fiber-waveguide coupling η_f was calculated to be approximately 20% by using the finite-difference method (FDM) based on a commercial photon design suite FIMMPROP. With an estimated minimum focused optical spot size of 0.75 μm, such poor fiber-waveguide coupling efficiency is considered to be caused by the large difference of the modal field distribution between the focused fiber mode and the membrane waveguide mode. The simulation result indicated that the responsivity of the device (considering η_{wg} and η_c) was 0.95 A/W. Saturation of the photocurrent due to carrier accumulation was observed under a bias voltage of 0 V.

Figure 5 provides the absorption-length-dependent R_{ex} with different W_s under a bias voltage of −1 V. A wider stripe provides larger ξ to the GaInAs absorber, as can be seen in the mode field distribution. The theoretical curves based on Eq. (1) with an adjustable loss parameter ($\eta_f \eta_{wg} \eta_c \eta_i$), which describes the absolute maximum value of the curve, the calculated value of ξ for different W_s, and a fixed material absorption coefficient α of 5000 cm^{-1}, which depends on the inclination of the responsivity curve, fit well with the experiment plots. (The theoretical curves based on different α and different loss parameters are provided in Appendix A for comparison.) The reduction in R_{ex} of the device with W_s of 0.5 μm is caused by the drastic decrease in η_{wg} of the large mode field in the narrow waveguide, which suffers greatly from the absorption loss in the heavily doped *p*-InP side clad ($\alpha = 8\ \mathrm{cm}^{-1}$) and the scattering loss. The theoretical curves indicate that absorption efficiency above 90% can be achieved for a PD with a length of 10 μm and W_s larger than 0.7 μm.

With an estimated sufficient absorption length of approximately 10 μm, we have also investigated the junction capacitance of the PD by simply using the parallel-plate model. The junction capacitance, which is also identified as the depletion capacitance, is defined approximately as $C_j = \varepsilon_{\mathrm{GaInAs}} \cdot h \cdot L / W_s$, where $\varepsilon_{\mathrm{GaInAs}} = 13.9\varepsilon_0$ is the permittivity of the GaInAs, $h = 0.27$ μm is the thickness of the *p-i-n* junction that equals to the thickness of the core layer, and $L = 10$ μm is the junction length or the estimated absorption length. The width of the depletion layer is considered the same as the stripe width W_s with an assumption of the full depletion of the absorption layer when applying the bias voltage. The calculated parallel-plate capacitance is less than 0.5 fF for W_s larger than 0.7 μm. It is considered a sufficiently small value for fulfilling the predicted requirements of on-chip photodiodes, which suggested that a device capacitance of less than 1 fF is required for a *p-i-n* PD to be connected with a load resistor larger than 10 kΩ, providing a cutoff frequency exceeding 10 GHz and an output voltage of several hundred mV with an input light signal on the order of fJ/bit level [24]. Actually, the parasitic capacitance of the electrical pad should also be considered part of the device capacitance with the current structure. However, it could be removed when the PD is introduced into the on-chip photonic integrated circuit that we do not need to use the probes for measurement.

Based on the estimated C_j, the cutoff frequency of our PD has also been investigated by using the same method for ensuring that it can match the modulation speed of the on-chip membrane laser when connected to a high-load resistor [30]. The cutoff frequency can be described as $f_{3\mathrm{dB}}^{-2} = f_{\mathrm{RC}}^{-2} + f_{\mathrm{TT}}^{-2}$, where $f_{\mathrm{RC}} = (2\pi(R_L + R_s)C_j)^{-1}$ is the RC bandwidth, $R_L = 10$ kΩ is the load resistance, and R_s is the sheet resistance, which is strongly related to the distance between the absorber and the electrodes W_d, and f_{TT} is the transit frequency, which corresponds to the carrier transition time as a function of the stripe width W_s, the hole saturation drift velocity, its mobility, and the assumed applied bias voltage of −1 V

in consideration of the supply voltage of the recent CMOS LSI. As a result, a maximum cutoff frequency $f_{3\,\mathrm{dB}}$ of 19.4 GHz can be expected with $W_s = 0.7$ μm, which is more than sufficient for the high-speed on-chip optical interconnection.

B. Photonic-Crystal-Waveguide-Type GaInAs/InP *p-i-n* PD

PhC is considered one of the promising solutions for the realization of ultra-compact optical devices. The enhancement of light-matter interactions such as gain and loss can be induced by the extremely strong optical confinement or the slow light effect within a well-designed PhC structure. Specifically, an increased absorption per length can be obtained by embedding the compact GaInAs bulk into the defect region of the in-plane PhC waveguide. The measured responsivity R_{ex} of the PhC-PD can be rewritten as the following Eq. (2):

$$R_{ex} = \eta_f \cdot \eta_{wg} \cdot \eta_c \cdot \eta_i \cdot \frac{q}{h\nu} \cdot (1 - e^{-A\xi\alpha L}), \tag{2}$$

where A is an additional parameter that represents the enhancement factor of the absorption induced by the PhC.

The measured R_{ex} of the PhC-PDs with different W_s and L are plotted in Fig. 6. The dark current of the PhC-waveguide-type PD with $W_s = 0.7$ μm and $L = 30$ μm was found to be 5.5 μA at a reverse bias of 1 V. The same value as the conventional-waveguide-type PD mentioned in Section 3.A indicated that the formation of air holes in cladding layers did not cause an apparent increase of the nonradiative surface recombination. A comparison of the calculated propagation modes in the absorber-embedded PhC waveguide region and conventional waveguide region by using the 3D-FDTD method is illustrated in Fig. 7. We have reported before that a single-line-defect PhC waveguide in our membrane structure is able to shorten the absorption length L by half (compared to the conventional-waveguide-type PD) because of the slow-light effect, which is related to a slow-down factor $S = n_g/n$ (n is the refractive index of the material). The relative W_s of the GaInAs bulk in such a design would be 0.3 μm, which is 0.4-μm narrower than the basic line width $W_0 = \sqrt{3}a$, defined as the removal of one row of air holes. In the case of $W_s = 0.5$ μm, the line defect width of the PhC will be approximately $1.3W_0$ and performs as a multimode waveguide. The shorter L can accordingly be attributed to the enhancement of the lateral optical confinement instead of the slow-light effect, as can be seen in the comparison shown in Fig. 7(a). When W_s is increased to 0.7 μm, the corresponding width of the PhC waveguide will be approximately $1.5W_0$, and it is mathematically determined that a single-mode window would open up again by using a commercial photonic band solver. It was considered a common phenomenon in membrane-type waveguides [31], which indicated that the slow-down factor S would again become the dominant factor affecting the enhancement of absorption per length, as seen in Fig. 7(b). The case of $W_s = 0.9$ μm with a line defect width of $1.8W_0$ of the PhC waveguide, as shown in Fig. 7(c), is the same as that of $W_s = 0.5$ μm. The reduction in the measured responsivity R_{ex} was observed in comparison with the conventional waveguide-type PD, which is considered to be attributed to the decreased η_c induced by the scattering loss and reflection loss within the interface between the GaInAs-embedded PhC waveguide and the GaInAsP passive waveguide.

The PhC enhancement factor A related to different W_s was introduced here for assessing the absorption enhancement induced by the PhC, which is dominated by either the slow-light effect or the improvement of the optical confinement in lateral direction. The factor that depends on the inclination of the R_{ex} curve, as explained before, was extracted from the fitting curves of the experimental data based on Eq. (2), and the results are shown in Fig. 8. It should be noted that during the fitting,

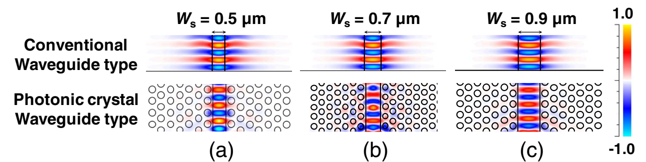

Fig. 7. Simulation results of the propagation modes in conventional-waveguide-type PD and photonic-crystal-waveguide PD based on 3D-FDTD method. (a) $W_s = 0.5$ μm, (b) $W_s = 0.7$ μm, and (c) $W_s = 0.9$ μm.

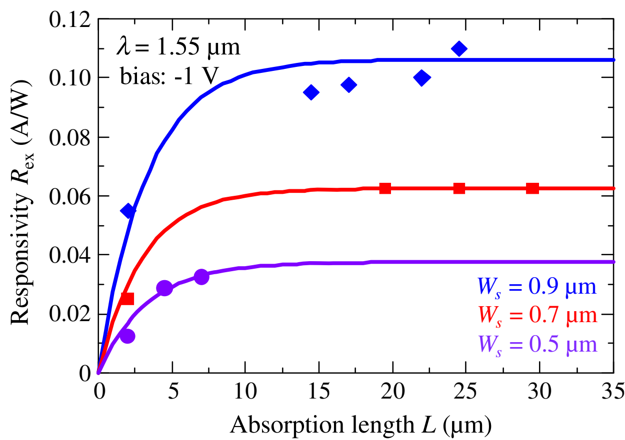

Fig. 6. Experimental plots and theoretical curves of R_{ex} of photonic-crystal-waveguide-type PD against absorption length at 1.55 μm with different stripe widths W_s.

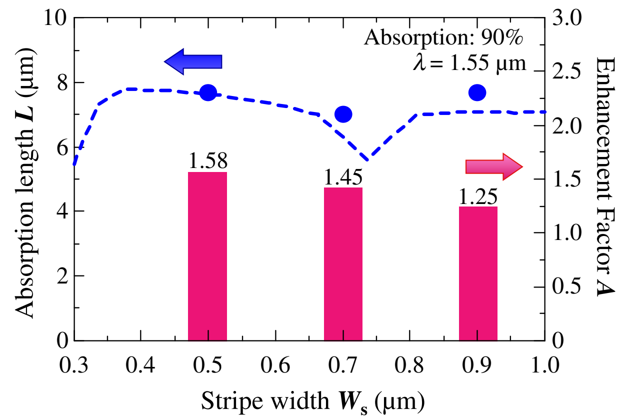

Fig. 8. Bar: Extracted PhC enhancement factor A from fitting curves. Dashed line: Calculated absorption length L of the PhC-WG based on 3D-FDTD. Dots: Theoretical L of Eq. (2) based on extracted A.

Table 1. Comparison of Waveguide-Integrated PDs on Si/SOI Platform

Absorption Material	Waveguide Material	Device Structure[b]	Absorption Length (μm)	Absorption Volume (μm^3)	λ_{in} (μm)	DC Response (A/W)	Year	References
Ge	Si	Vertical PIN	30	72	1.55	1.00	2017	[32]
Ge	Si	Lateral PIN	4.0	5.2	1.50	0.80	2011	[18]
Ge	Si	APD	10	1.1	1.50	0.15	2010	[19]
Si/Ge	Si	UTC	90	4.7	1.55	0.70	2014	[33]
MQW	GaInAsP	Lateral PIN	200	4.2	1.55	0.80	2011	[26]
InGaAs	InP	MSM	29	232	1.55	0.19	2016	[34]
InGaAs	Si	MUTC	35	182	1.55	0.95	2016	[35]
InGaAs	InP	Vertical PIN	10	35	1.58	0.45	2010	[36]
InGaAs	GaInAsP	Lateral PIN	30 ([a]10)	2.5 ([a]0.8)	1.55	0.95	—	This work
InGaAs	GaInAsP	PhC PIN	25 ([a]7.0)	2.1 ([a]0.6)	1.55	0.31	—	This work

[a]Estimated value for a 90% absorption of the incident light.
[b]APD, avalanche photodiode; UTC, uni-traveling carrier photodiode; MSM, metal-semiconductor-meta; MUTC, modified uni-traveling carrier photodiode.

we assumed that the material absorption coefficient α of 5000 cm^{-1} did not change with the introduction of the PhC structure. The corresponding theoretical absorption length L based on the extracted A, which provides a light absorption of 90%, was also plotted in the figure along with the simulation result using the 3D-FDTD method with a 1550-nm continuous-wave input light (dashed line). The valley near $W_s = 0.7$ μm can be explained by the reopened single-mode window of the $1.5W_0$ PhC waveguide, as mentioned before. A good agreement was confirmed between the FDTD simulation result and the theoretical value, which proves the validity of the obtained experimental data. In conclusion, it is predicted that the device length of the PD for a 90% light absorption can be shortened to 7 μm with the aid of the in-plane PhC structure. With the shortened absorption length of 7 μm, the junction capacitance C_j was calculated to be approximately 0.3 fF, based on the parallel-plate model. However, an increase of the sheet resistance caused by the smaller device size and the formation of air holes in the p-InP and n-InP clad layers should be taken into consideration during the estimation of the cutoff frequency. Yet, we still obtained an increased $f_{3\,dB}$ of 21 GHz thanks to the reduction of device size. It is believed that a further increase of the $f_{3\,dB}$ can be realized with shorter absorption length of the PD by adopting the slow-light effect of the PhC structure.

Finally, the experimental results of the waveguide-integrated PDs on the Si/SOI platform, which were demonstrated in recent years, are summarized in Table 1 for comparison. In terms of our conventional waveguide-type PD, a relatively short absorption length and an extremely small absorber volume can provide a satisfactory responsivity to the 1.55-μm input. A shorter device length, which enables an absorption efficiency of 90%, is obtained because of the PhC structure. However, a well-designed coupling interface between the passive waveguide region and the PD region is necessary to improve the responsivity [37,38]. In addition, slow-light PhC-PD, which can be expected to result in a further size reduction of the PD, will be investigated in the future for the fabrication of small-scale PDs.

4. CONCLUSION

Comparison of two kinds of GaInAs/InP waveguide-type p-i-n PDs with different stripe widths and absorption lengths was demonstrated. In the case of the conventional-waveguide-type PD, a high responsivity of 0.95 A/W at 1.55-μm wavelength was estimated with the device length of 30 μm and stripe width of 0.7 μm. Curve fitting of the experimental results indicated that absorption efficiency above 90% could be expected with a 10-μm device length. Results for the PhC-waveguide-type PD fit well with the simulation result using the 3D-FDTD method. It proves the feasibility of designing devices with lengths shorter than 7 μm by embedding the GaInAs bulk into the defect region of an in-plane PhC waveguide. A well-designed coupling structure between the butt-jointed passive waveguide and the PhC region will be required for improving the responsivity. A strong slow-light effect should be applied to the design for a further size reduction, leading to an expected smaller device capacitance and higher 3-dB frequency.

APPENDIX A: DETAILS OF CURVE FITTING OF EXPERIMENTAL DATA

The theoretical curves of R_{ex} based on Eq. (2) with different loss parameters $\eta_f, \eta_{wg}, \eta_c$, and η_i are illustrated in Fig. 9 for comparison. Fitting of the experimental data started with the adjustment of the loss parameters, which determine the absolute maximum value of the responsivity. This maximum value represents the saturation of light absorption within a sufficient absorption length. The material absorption coefficient

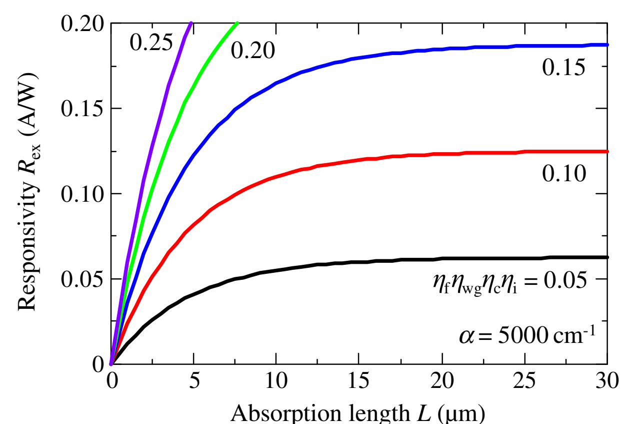

Fig. 9. Theoretical curves of R_{ex} based on different loss parameters $\eta_f\eta_{wg}\eta_c\eta_i$ with a fixed α.

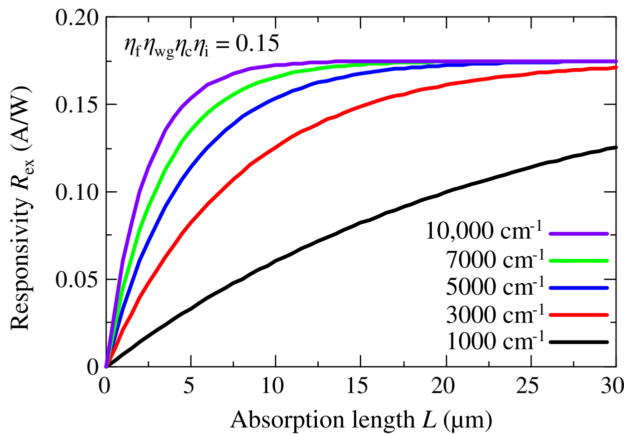

Fig. 10. Theoretical curves of R_{ex} based on different absorption loss α with a fixed loss parameter $\eta_f\eta_{wg}\eta_c\eta_i$.

α of GaInAs in the exponential function in Eq. (2), which determines the inclination of the theoretical curve, was then adjusted for fitting the experimental data, as shown in Fig. 10. In the case of the conventional-waveguide-type PD, the calculated confinement factor ξ based on the FDM method was used in the theoretical formula. We found that a material absorption coefficient α of 5000 cm^{-1} would be an appropriate result for fitting all the experimental data with different values of the stripe width W_s. In the case of the PhC-waveguide-type PD, α was assumed the same as that of the conventional-waveguide-type PD, and the enhancement factor A was adjusted for obtaining an appropriate inclination of the theoretical curve.

Funding. Japan Society for the Promotion of Science (JSPS) (15H05763, 15J11776, 16H06082, 16J11581, 17H03247); Core Research for Evolutional Science and Technology (CREST) (PMJCR15N6).

REFERENCES

1. M. Kada, "Development of functionally innovative 3D-integrated circuit (dream chip) technology/high-density 3D-integration technology for multifunctional devices," in *IEEE International Conference on 3D System Integration (3DIC)* (IEEE, 2009), pp. 1–6.
2. A. Fazzi, R. Canegallo, L. Ciccarelli, L. Magagni, F. Natali, E. Jung, P. Rolandi, and R. Guerrieri, "3-D capacitive interconnections with mono- and bi-directional capabilities," IEEE J. Solid-State Circuits **43**, 275–284 (2008).
3. K. Niitsu, Y. Shimazaki, Y. Sugimori, Y. Kohama, K. Kasuga, I. Nonomura, M. Saen, S. Komatsu, K. Osada, N. Irie, T. Hattori, A. Hasegawa, and T. Kuroda, "An inductive-coupling link for 3D integration of a 90 nm CMOS processor and a 65 nm CMOS SRAM," in *IEEE Solid-State Circuits Conference Digest of Technical Papers (ISSCC)* (IEEE, 2009), pp. 480–481.
4. D. A. B. Miller, "Device requirements for optical interconnects to silicon chips," Proc. IEEE **97**, 1166–1185 (2009).
5. K. Ohashi, K. Nishi, T. Shimizu, M. Nakada, J. Fujikata, J. Ushida, S. Torii, K. Nose, M. Mizuno, H. Yukawa, M. Kinoshita, N. Suzuki, A. Gomyo, T. Ishi, D. Okamoto, K. Furue, T. Ueno, T. Tsuchizawa, T. Watanabe, K. Yamada, S. Itabashi, and J. Akedo, "On-chip optical interconnect," Proc. IEEE **97**, 1186–1198 (2009).
6. C. Sun, M. T. Wade, Y. Lee, J. S. Orcutt, L. Alloatti, M. S. Georgas, A. S. Waterman, J. M. Shainline, R. R. Avizienis, S. Lin, B. R. Moss, R. Kumar, F. Pavanello, A. H. Atabaki, H. M. Cook, A. J. Ou, J. C. Leu, Y. Chen, K. Asanović, R. J. Ram, M. A. Popović, and V. M. Stojanović, "Single-chip microprocessor that communicates directly using light," Nature **528**, 534–538 (2015).
7. D. Liang, G. Roelkens, R. Baets, and J. E. Bowers, "Hybrid integrated platforms for silicon photonics," Materials **3**, 1782–1802 (2010).
8. R. Chen, K. W. Ng, W. S. Ko, D. Parekh, F. Lu, D. T. Thai-Truong, K. Li, and C. Chang-Hasnain, "Nanophotonic integrated circuits from nanoresonators grown on silicon," Nat. Commun. **5**, 4325 (2014).
9. S. Arai, N. Nishiyama, T. Maruyama, and T. Okumura, "GaInAsP/InP membrane lasers for optical interconnects," IEEE J. Sel. Top. Quantum Electron. **17**, 1381–1389 (2011).
10. J. J. G. M. Van der Tol, J. J. Pello, S. S. Bhat, Y. Y. Jiao, D. D. Heiss, G. G. Roelkens, H. H. Ambrosius, and M. M. Smit, "Photonic integration in indium-phosphide membranes on silicon (IMOS)," Proc. SPIE **8988**, 89880M (2014).
11. D. Inoue, J. Lee, K. Doi, T. Hiratani, Y. Atsuji, T. Amemiya, N. Nishiyama, and S. Arai, "Room-temperature continuous-wave operation of GaInAsP/InP lateral-current-injection membrane laser bonded on Si substrate," Appl. Phys. Express **7**, 072701 (2014).
12. D. Inoue, T. Hiratani, K. Fukuda, T. Tomiyasu, T. Amemiya, N. Nishiyama, and S. Arai, "High-modulation efficiency operation of GaInAsP/InP membrane distributed feedback laser on Si substrate," Opt. Express **23**, 29024–29031 (2015).
13. T. Hiratani, D. Inoue, T. Tomiyasu, Y. Atsuji, K. Fukuda, T. Amemiya, N. Nishiyama, and S. Arai, "Room-temperature continuous-wave operation of membrane distributed-reflector laser," Appl. Phys. Express **8**, 112701 (2015).
14. C. Debaes, A. Bhatnagar, D. Agarwal, R. Chen, G. A. Keeler, N. C. Helman, H. Thienpont, and D. A. B. Miller, "Receiver-less optical clock injection for clock distribution networks," IEEE J. Sel. Top. Quantum Electron. **9**, 400–409 (2003).
15. S. Assefa, F. Xia, W. M. Green, C. L. Schow, and Y. A. Vlasov, "CMOS-integrated optical receivers for on-chip interconnects," IEEE J. Sel. Top. Quantum Electron. **16**(5), 1376–1385 (2010).
16. J. E. Proesel, B. G. Lee, A. V. Rylyakov, C. W. Baks, and C. L. Schow, "Ultra-low-power 10 to 28.5 Gb/s CMOS-driven VCSEL-based optical links," J. Opt. Commun. Netw. **4**, B114–B123 (2012).
17. J. Kim and J. F. Buckwalter, "A 40-Gb/s optical transceiver front-end in 45 nm SOI CMOS," IEEE J. Solid-State Circuits **47**, 615–626 (2012).
18. C. T. DeRose, D. C. Trotter, W. A. Zortman, A. L. Starbuck, M. Fisher, M. R. Watts, and P. S. Davids, "Ultra compact 45 GHz CMOS compatible germanium waveguide photodiode with low dark current," Opt. Express **19**, 24897–24904 (2011).
19. S. Assefa, F. Xia, and Y. A. Valsov, "Reinventing germanium avalanche photodetector for nanophotonic on-chip optical interconnects," Nature **464**, 80–84 (2010).
20. L. Cao, J. S. Park, P. Fan, B. Clemens, and M. L. Brongersma, "Resonant germanium nanoantenna photodetectors," Nano Lett. **10**, 1229–1233 (2010).
21. R. Chen, D. Parekh, K. W. Ng, and C. Chang-Hasnain, "High-speed avalanche photodiodes using III-V nanopillars monolithically grown on silicon," in *IEEE Group IV Photonics (GFP)* (IEEE, 2012), pp. 48–50.
22. J. Guo, Z. Wu, Y. Li, and Y. Zhao, "Design of plasmonic photodetector with high absorptance and nano-scale active regions," Opt. Express **24**, 18229–18242 (2016).
23. T. Baba, "Slow light in photonic crystals," Nat. Photonics **2**, 465–473 (2008).
24. K. Nozaki, S. Matsuo, K. Takeda, T. Sato, E. Kuramochi, and M. Notomi, "InGaAs nano-photodetectors based on photonic crystal waveguide including ultracompact buried heterostructure," Opt. Express **21**, 19022–19028 (2013).
25. K. Nozaki, S. Matsuo, T. Fujii, K. Takeda, M. Ono, A. Shakoor, E. Kuramochi, and M. Notomi, "Photonic-crystal nano-photodetector with ultrasmall capacitance for on-chip light-to-voltage conversion without an amplifier," Optica **3**, 483–492 (2016).
26. T. Okumura, D. Kondo, H. Ito, S. Lee, T. Amemiya, N. Nishiyama, and S. Arai, "Lateral junction waveguide-type photodiode grown on semi-insulating InP substrate," Jpn. J. Appl. Phys. **50**, 020206 (2011).
27. T. Shindo, T. Koguchi, M. Futami, K. Doi, Y. Yamahara, J. Lee, T. Amemiya, N. Nishiyama, and S. Arai, "10 Gbps operation of top air-clad lateral junction waveguide-type photodiodes," Jpn. J. Appl. Phys. **52**, 118002 (2013).

28. D. Inoue, T. Hiratani, Y. Atsuji, T. Tomiyasu, T. Amemiya, N. Nishiyama, and S. Arai, “Monolithic integration of membrane-based butt-jointed built-in DFB lasers and PIN photodiodes bonded on Si substrate,” IEEE J. Sel. Top. Quantum Electron. **21**, 1502907 (2015).
29. D. Inoue, J. Lee, T. Shindou, M. Futami, K. Doi, T. Amemiya, N. Nishiyama, and S. Arai, “Butt-joint built-in (BJB) structure for membrane photonic integration,” in *IEEE International Conference on Indium Phosphide and Related Materials (IPRM)* (IEEE, 2013), paper TuD3-6.
30. Z. Gu, T. Hiratani, T. Amemiya, N. Nishiyama, and S. Arai, “Study of a slow-light-enhanced membrane photodetector for realizing on-chip interconnection with low power consumption,” J. Opt. Soc. Am. B **34**, 440–446 (2017).
31. M. Galli, D. Bajoni, M. Patrini, G. Guizzetti, D. Gerace, L. C. Andreani, M. Belotti, and Y. Chen, “Single-mode versus multimode behavior in silicon photonic crystal waveguides measured by attenuated total reflectance,” Phys. Rev. B **72**, 125322 (2005).
32. K. Ito, T. Hiraki, T. Tsuchizawa, and Y. Ishikawa, “Waveguide-integrated vertical pin photodiodes of Ge fabricated on p+ and n+ Si-on-insulator layers,” Jpn. J. Appl. Phys. **56**, 04CH05 (2017).
33. M. Piels and J. E. Bowers, “40 GHz Si/Ge uni-traveling carrier waveguide photodiode,” J. Lightwave Technol. **32**, 3502–3508 (2014).
34. Y. Cheng, Y. Ikku, M. Takenaka, and S. Takagi, “Low-dark-current waveguide InGaAs metal-semiconductor-metal photodetector monolithically integrated with InP grating coupler on III-V CMOS photonics platform,” Jpn. J. Appl. Phys. **55**, 04EH01 (2016).
35. X. Xie, Q. Zhou, E. Norberg, M. Jacob-Mitos, Y. Chen, Z. Yang, A. Ramaswamy, G. Fish, J. C. Campbell, and A. Beling, “High-power and high-speed heterogeneously integrated waveguide-coupled photodiodes on silicon-on-insulator,” J. Lightwave Technol. **34**, 73–78 (2016).
36. P. R. A. Binetti, X. J. M. Leijtens, T. De Vries, Y. S. Oei, L. D. Cioccio, J.-M. Fedeli, C. Lagahe, J. Van Campenhout, D. Van Thourhout, P. J. Van Veldhoven, R. Nötzel, and M. K. Smit, “InP/InGaAs photodetector on SOI photonic circuitry,” IEEE Photon. J. **2**, 299–305 (2010).
37. C. Lin, X. Wang, S. Chakravarty, B. S. Lee, W. Lai, and R. T. Chen, “Wideband group velocity independent coupling into slow light silicon photonic crystal waveguide,” Appl. Phys. Lett. **97**, 183302 (2010).
38. M. Askari and A. Adibi, “High efficiency coupling of light from a ridge to a photonic crystal waveguide,” Appl. Opt. **52**, 5803–5815 (2013).

131.112.10.207 {ts '2017-09-22 21:24:49'}